

---

# Investigation of Neutron Diffusion in H<sub>2</sub>O

A University of Birmingham Lab Report

By Benjamin Crump, Principal Nuclear Engineer at BAE Systems, Inc.

For the MSc Physics & Technology of Nuclear Reactors

**May 6, 2022.**

---

## Abstract

An investigation of Neutron diffusion behaviour within a water tank containing light water was carried out with BF<sub>3</sub> and <sup>3</sup>He detectors. The total and fast neutron fluxes were measured by use of a Cadmium shield placed around the detector(s). A two-group diffusion scheme fit was made on the flux against distance plots in order to determine the diffusion length and age of thermal and fast neutrons respectively, a simple MCBEND model was also used to model the behaviour of the diffusion theory fit near the tank wall. A thermal neutron diffusion length was found to be 26.16 +/- 0.46 mm, and fast neutron age was 4616 +/- 102.4mm<sup>2</sup>.

## 1 Introduction

Free neutrons interact with surrounding materials (moderators) through the process of collision (moderation), until they attain thermal equilibrium with the atoms of the moderator. In a nuclear reactor for example, fast neutrons that are emitted from the fission process are thermalised by moderator. At this energy range (approx 0.025eV) neutrons diffuse into regions of lower concentrations, analogous to the behaviour of gas molecules. There is also an increased probability of the neutron being captured by the surrounding nuclei. The balance of these two processes determines the diffusion length ( $L$ ) in a given moderator. The aim of this experiment is to measure the diffusion length of thermal neutrons within a water tank containing light water ( $H_2O$ ) using a two group diffusion scheme. This will

be done by measuring the thermal neutron flux at various distances from a source of neutrons (1 Ci AmBe source) using a  $\text{BF}_3$  detector and then compared with a  $^3\text{He}$  detector (for verification). The  $\text{BF}_3$  detector shall be investigated initially and an operating voltage shall be chosen. Next, the neutron flux will be measured at various distances and heights from the source at the centre of the water tank. The resultant flux distribution shall be fitted to the expected values as predicted by diffusion theory. A simplified MCBEND simulation shall also be carried out in order to observe how diffusion theory in the presence of a surface, where measurements may not reach.

## 2 Theory

### 2.1 Neutron Production

Neutrons are particles of neutral charge and of mass 1.0086647 amu [8] (slightly greater than that of a proton). Unbound to an atom (free) they have a half-life of around 10.3 minutes before  $\beta^-$  decaying as follows:  $n \rightarrow p + e^- + \bar{\nu}$ . The source for this experiment is an AmBe neutron source.  $^{241}\text{Am}$  has a half life of 432.6 years and alpha decays 100% of the time, as shown by Equation 1.



The resulting alpha particle carries away a share of the energy released from this reaction, given by  $Q(A - 4)/A$ .  $^{241}_{95}\text{Am}$  predominately releases alpha particles of two energies, one at an energy of 5.48 MeV (84.8%) and the other with an energy of 5.44 MeV (13.1%) [3]. Given sufficient energy, the alpha particles can overcome the Coulomb barrier and be absorbed by the Beryllium (Be) fill gas causing it to undergo the  $(\alpha, n)$  reaction (primarily) shown by Equation 2.



Knoll [12] states that all average neutron energy spectra from any alpha-Beryllium sources are very similar. A plot of the energy spectrum from a AmBe source is shown on Figure 1 [1]. A number of features are visible on this plot, many can be attributed to the daughter product ( $^{12}\text{C}$ ) being emitted at its lowest energy states

(via inelastic scattering with the  $\alpha$ ) and de-exciting with  $\gamma$  emission. The plot also shows a number of comparisons made by Bedogni et al, including the ISO 8529-1 [11] standard, MCNP Monte-carlo simulation results, and the SOURCES 4C ORNL code.

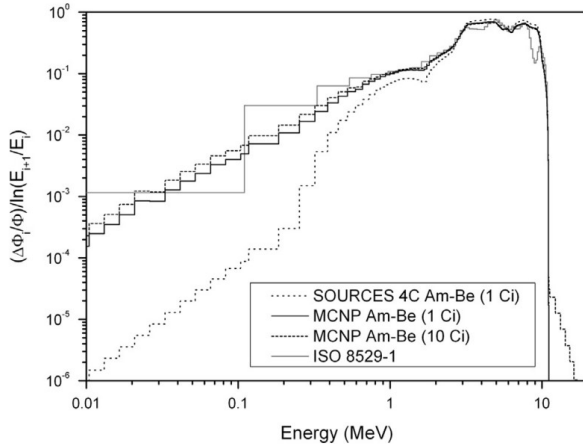


**Figure 1:** AmBe Neutron Source Energy Spectrum

## 2.2 Neutron Diffusion

This report shall not derive the relevant equations for one and two-group neutron diffusion calculations, Lamarsh & Baratta pp.259 [13], and Duderstadt & Hamilton [6] provide further detail. The one-group neutron equation can be easily modified to reflect the fast (only) neutron flux by including the fast neutron Fermi age ( $\tau_{Fast}$ ) as shown by Equation 3. A single constant ( $A$ ) may be used to replace the thermal group constants of which are unknown for this experimental set-up, using Equation 4 this constant may then be used for the fitting of the measured neutron flux. Equation 3 may then be modified in order to include the thermal neutrons, i.e. Equation 5. Again, the fast group constants are unknown at this point and those group constants are to be replaced by a single constant ( $C$ ), shown by Equation 6. This will enable the fitting of the neutron flux and determination of the diffusion length ( $L$ ). Given that the group constants and variables within the single constant  $A$  are all positive it is anticipated that constant  $A$  will be a positive integer. The same cannot be said for the constant  $C$ , due to the negative contribution of  $\tau$  on the denominator; constant  $C$  should be negative. The diffusion length ( $L$ ) is related to

the mean square distance travelled (as the crow flies) by thermal neutrons within a given medium before absorption, as demonstrated by Equation 7. For fast neutrons, the parameter  $\tau$  is related to the mean square distance travelled before it slows to thermal equilibrium (Equation 8). In reactor core design, it is often convenient to combine these two factors and express as a migration length ( $M$ ) (Equation 9).

$$\phi_F(r) = \frac{S \tau_F}{4 \pi r^2 D_F \tau_F^2} e^{-r/\sqrt{\tau_F}} \quad (3)$$

$$\phi_F(r) = \frac{A}{r} e^{-r/\sqrt{\tau_F}} \quad (4)$$

$$\phi_T(r) = \frac{S L_T^2}{4 \pi r D (L_T^2 - \tau_T)} \frac{e^{-r/L_T} - e^{-r/\sqrt{\tau_T}}}{r} \quad (5)$$

$$\phi_T(r) = C \frac{e^{-r/L_T} - e^{-r/\sqrt{\tau_T}}}{r} \quad (6)$$

$$L^2 = \frac{1}{6} \overline{r^2} \quad (7)$$

$$L_s^2 = \tau = \frac{1}{6} \overline{r^2} \quad (8)$$

$$M = \sqrt{L^2 + L_s^2} = \sqrt{L^2 + \tau} \quad (9)$$

where,

$\phi$  Neutron flux  $S$  is the source emission rate

$r$  is the target radius from the source  $D$  is the diffusion coefficient

$L$  is the diffusion length  $\tau$  is the Neutron age

### 2.2.1 Predicted Results

The diffusion length ( $L$ ) changes with the density of the medium, which in turn changes with temperature. The temperature of the tank water will likely be approximately 17 to 22 °C during these measurements i.e. ambient. The temperature

was not actively measured within the tank, it is hypothesised that experimental and analytical errors would likely affect the precision of the fitted diffusion length, at least greater than the temperature corrections at the ambient temperature range. The diffusion length for thermal neutrons in  $H_2O$  is  $27.61 +/- 0.09$  mm. This value was retrieved from Holmes and Zerkle et al [9] of the US-based National Nuclear Laboratory, the study takes a weighted mean value of  $L$  from 12 different paper, measured at temperature of  $22^\circ C$ . These studies mostly use alternate neutron sources and different experimental set-ups, but gives a feel for the variation of neutron diffusion with moderator temperature.

Another factor in this experiment are small the voids of gas between the source and detectors and their respective outer tube, for this experiment the void fraction is assumed to be zero. Iqbal and Mirza et al [10] provide values for  $L$  and  $\tau$  of  $29.49 +/- 1.3$ mm and  $5871 +/- 260$ mm<sup>2</sup> (respectively), from a similar water-bath experiment with an AmBe neutron source, with cadmium shield, at zero void fraction, and ambient temperatures. A further factor which will not be considered are impurities within the tank water, tap water will be used in this experiment as opposed to reactor grade water. These figures will later be compared with MCBEND (Monte-Carlo) simulation results produced in this report. According to Lamarch & Baratta [13], it is already anticipated that the experimental (fitted) values shan't be exact, the two-group calculation used herein (Equation 6) is good as a simple, but rough, approximation for the slowing of neutrons from an assumed point source.

### **2.2.2 Boundary Conditions**

The diffusion equation is derived from Fick's laws of diffusion, as detailed in Lamarch & Baratta [13]. Fick's law is not valid in the immediate vicinity of a surface as illustrated by Figure 2. For this experiment there must obviously be a container with a boundary surface to contain the water. This container is many times larger than the typical diffusion length or area, and considering the moderator (water) to be a infinite medium would be a reasonable assumption. the measurements taken close to the source and outer tank surface may need to be disregarded by extrapolation distance ( $d$ ), given by Equation 10. The density of the medium is comparably large and therefore  $L>>D$ , this affect may not then be measurable.

$$d = 2.14D \quad (10)$$

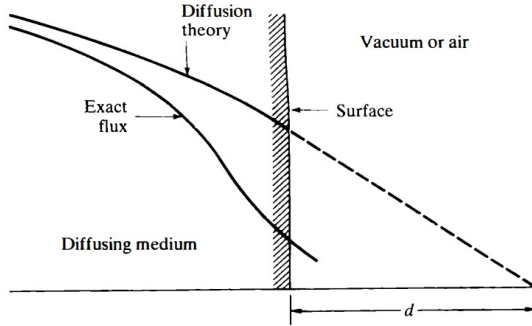


**Figure 2:** Surface extrapolation distance and diffusion treatment.

### 2.2.3 Cadmium Shield

In order to conduct a two group fit a method of filtering out the thermal or fast neutrons in order to distinguish between both groups, for this experiment a Cadmium sheath is to be placed around the detector. Cadmium has a high absorption cross section for thermal neutrons as shown by Figure 3 (retrieved from EDNF [15]) with a severe drop in absorption cross section at around 0.5 eV.

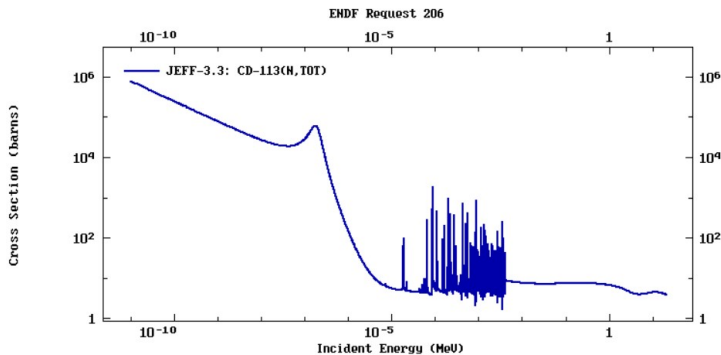


**Figure 3:** Cadmium shield neutron absorption cross-section.

## 2.3 Neutron Detector Properties

The detectors used in this experiment are types of gas-filled proportional counters. When an electric field is applied across the anode (central internal wire) and cathode (cylindrical outer casing of radius ' $r$ ') electrons and ions, produced by in-

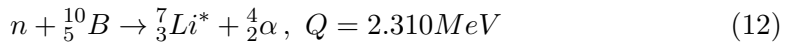
incident radiations upon the fill gas, migrate towards their respective electrodes. At sufficient applied voltages, gas multiplication will occur and the ion-pair charge is amplified significantly in order to produce an output signal for the pre-amplifier. The electric field between the anode and cathode is proportional to a  $1/r$  relation [12]. Electrons are clearly more mobile than the ions, as such the electrons are able to accelerate to much achieve energies. When this electron energy becomes greater than the binding energy of the atoms of the fill gas, an additional ion pair may be created, this then may go on to create further electron-ion pairs. This is known as the "avalanche" effect and occurs in a small area close to the central anode wire. Proportional detectors such as this often have a good signal to noise ratio when compared to other radiation detectors, due to this charge amplification effect [12]. The pulse size contribution of the electrons traveling to the anode wire is small, since they only travel a short distance to collect. To fully collect these ions takes a long time period, despite this most of the pulse is established due to the ion motion toward the cathode. Not waiting for these ions to fully arrive at the cathode means that a fraction of the pulse is lost, this is known as ballistic deficit [12]. This is quite an insignificant effect and the pulse generated is still proportional to the energy deposited in the detector volume. Due to the aforementioned effects there are different operating regions throughout the range of applied voltages. For this experiment the proportional region is required to achieve the desired pulse amplitude through charge amplification, therefore applied voltage should remain constant throughout to ensure consistent measurements. Figure 4a [12] illustrates the operating regions applicable to gas-filled detectors.

## 2.4 Neutron Detection

### 2.4.1 $\text{BF}_3$ Detector

The detector used for the experiment is a Boron Trifluoride ( $\text{BF}_3$ ) gas-filled proportional counter. Equation 11 outlines the two main  $(n,\alpha)$  reactions (including Q values) that occur when a neutron is incident upon this detector [12]. According to Knoll [12] these two reactions occur as a ratio of 94:6, i.e. 6% of the time to the ground state, the rest to the first excited state.





### 2.4.2 ${}^3He$ Detector

A Helium ( ${}^3He$ ) gas-filled detector was also used for comparative purposes, Equation 13 outlines the (n,p) reaction which makes neutron detection possible here.



### 2.4.3 The Wall Effect

Not all reactions will occur at the center of the detector and those that do not cause a visible effect on the spectra. This is known as the wall effect, illustrated by Figure 4b. The lowest of the two plateaus corresponds to the  $\alpha$  particle colliding with the detector wall and the  ${}^7Li$  depositing its' full energy in the fill gas. Here the energy deposited in the detector is a continuum between 4/11ths [12] of the Q-value and the full Q-value. The upper plateau is therefore due to the  ${}^7Li$  colliding with the wall and the  $\alpha$  particle depositing its' full energy in the fill gas. Where energy deposited is between 7/11ths [12] of and the full Q-value.

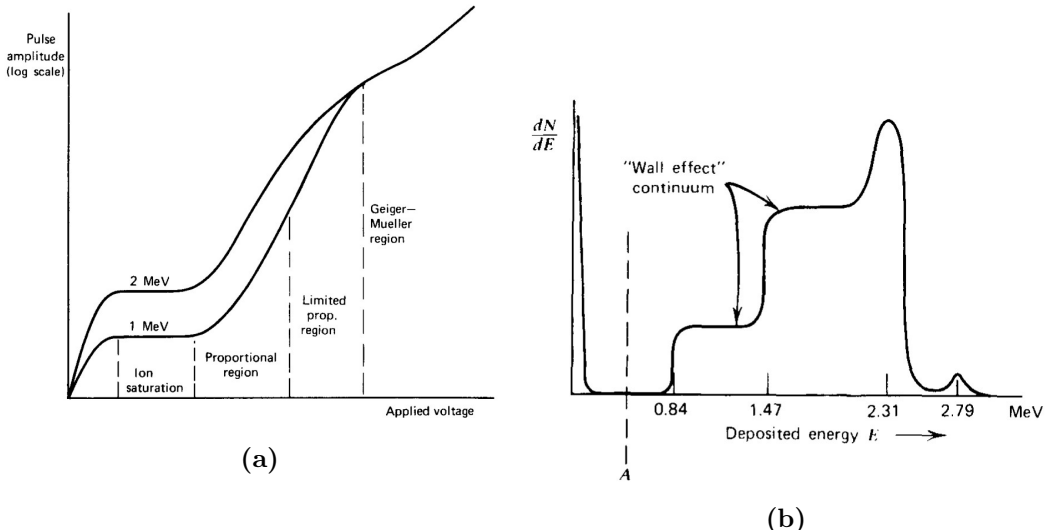


**Figure 4:** (a) Operating regions of gas-filled detectors [12]. (b) Expected spectra of  $BF_3$  detector including wall effect continuum [12].

### 3 Apparatus

#### 3.1 AmBe Neutron Source

According to the experiment description (university resource) the source is 1 Ci in strength, this equates to 37 GBq (disintegrations per second). A key document which outlines the expected data for this AmBe source is the ISO 8529-1 standard [11]. Source properties, retrieved from Knoll [12] and ISO 8529-1 [11], are outlined in Table 1. The neutron emission rate included therein is determined by Equation 15, this is an indicative figure in the absence of direct measurement via manganese sulfate solution gamma spectroscopy (or other method). Equation 14 calculates the number of  $10^6$  primary alpha particles (per second) emitted from a 1 Ci source.

$$\frac{37 \times 10^9}{10^6} = 37000 \quad (14)$$

Knoll [12] states that the neutron yield per  $10^6$  primary alphas is 82 (calculated) or 70 (experimental), with the latter experimental value being used in this case. Equation 15 finds the neutron emission rate in neutrons per second from a 1 Ci AmBe source. The neutron yield in this case is calculated to be  $2.59 \times 10^6$  neutrons per second.

$$70 \times 37000 = 2.59 \times 10^6 \quad (15)$$

Source	Half-life	Fluence-average Energy	Specific Source Emission Rate	Indicative Source Emission Rate
Am-Be	432.6 Years	4.17 MeV	$6 \times 10^{-5}$ /s/kg	$2.59 \times 10^6$ neutrons/s

**Table 1:** Source Properties Detailed

#### 3.2 Water Bath

The water bath is an approx.  $1\text{m}^3$  rainwater collection container manufactured by GRAF [7]. The outside measured dimensions of the tank are 104cm (dia) at the top and 117cm in height, the tank is not a uniform in diameter and tapers down at the bottom. Visually the material looks to be a type of Polypropylene plastic. The main central plastic tube contains the source which must not be removed from the

tank by students. There are measurement slides (in mm) with a movable plastic detector tube (void) on the radial (x) axis for more precise measurements of distance outward from the center of the tank (source location). The source is located 52.1cm off the bottom of the tank and approximately 53cm beneath the surface of the water. The detector tube bottom was set to be slightly lower than the center of the source (approx 6cm), this will effect the measurements and the crows' flight distance from the detector bottom to the source will be used to correct for axial measurements and the radial measurements taken at detector on bottom.

A factor considered earlier in the report was the effect of voids on the neutron diffusion, therefore it would be sensible to use only the radial measurements for fitting the diffusion length and area, given that a small but increasing void would be created below detector as it is pulled upward within the tube.

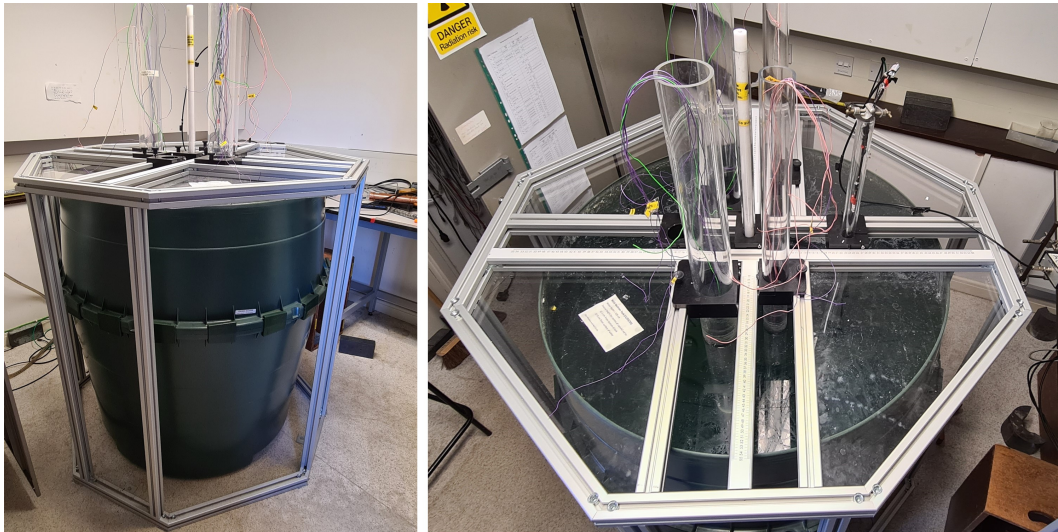


**Figure 5:** Neutron water bath

### 3.3 Detector Electronics

A labelled photograph (Figure 6) shows the modules installed in the NIM minibin for this experiment, the oscilloscope above (labelled 1), and the PC connected (labelled 5) via a multi-channel analyser (labelled 4).

The NHQ 212M power supply module (labelled 2) transforms the 24V/1A minibin supply to a maximum of 2kV to supply to the detector. The pre-amplifier is an

ORTEC 109PC low-noise charge-sensitive unit, located close to the detector (not in the minibin shown). This type of pre-amplifier integrates the detector charge pulse by means of a capacitor. A feedback resistor is employed so that the charge is integrated on the feedback capacitor can decay with a given time constant. The ORTEC 109PC pre-amplifier manual and brochure (Appendix A) are available on the author's shared repository [5] or on request.

The main amplifier is a Canberra Model 2020 spectroscopy amplifier module (labelled 3). This is used to amplify the pre-amplifier signal thereby generating a series of Gaussian shaped pulses through RC and CR networks (i.e. band pass filters). The shaping time can be used to reduce the thermal noise generated by the feedback resistor, benefiting resolution, although too high of a shaping time can affect the counting rates. A pile-up rejection circuit is provided to suppress the spectral distortion caused by pulses piling up at high count rates. Baseline restoration rate can also be set to 'auto' or 'high' to prevent the baseline shifting with the amplitude of the pulses, which can work to degrade resolution. The full Canberra Model 2020 product manual is available on the author's shared repository [5]. The two furthest right modules (unlabelled) are spare amplifier modules not used during this experiment. The MCA (labelled 4) and SCA (labelled 1) are explained in detail on a previous lab report, available on the author's shared repository [5].

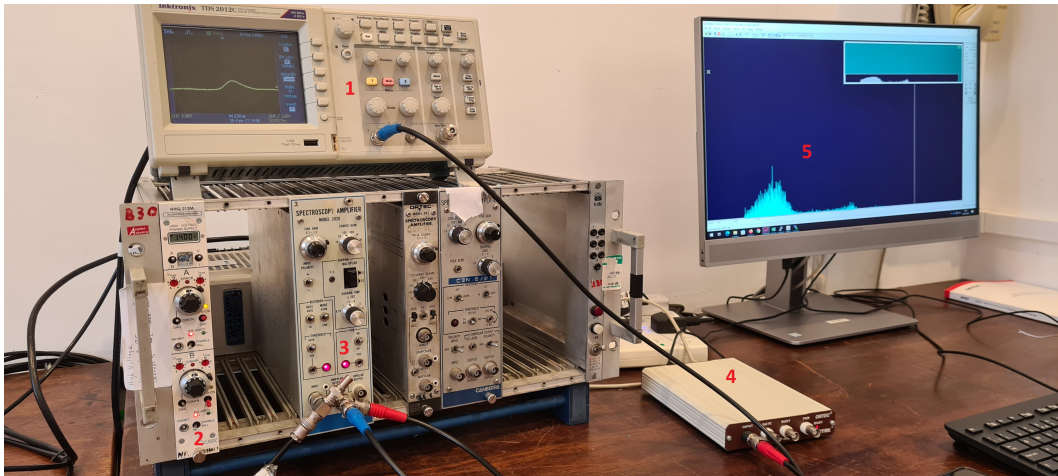


**Figure 6:** Photograph of detector electronics.

## 4 Method

### 4.1 Equipment Set-up

The equipment was connected as shown by Figure 7. The minibin and HV power module were switched on and the HV bias was slowly raised. The oscilloscope (SCA) was initially used to check the output of the detector was functional. Once content that a signal was being produced (approx. 600V) the MCA was connected and maestro was started on the PC. With a random gain and shaping time of 100 and  $1.5\ \mu\text{s}$  selected, the largest peak centroid position was recorded taken at every increase in 100V until a voltage of 2000V was reached. Replicating Figure 4a, the logarithm of the centroid was taken and plotted against the voltage, shown by Figure 8. Comparing Figure 4a and 8, a voltage of 1400V was appropriate to use to ensure that subsequent measurements were within the desired proportional region. The coarse gain was then adjusted to ensure all of the features lied within the channels available. A shaping time of  $1.5\mu\text{s}$  was selected as this gave a good resolution properties within a dead-time of approx. 5%.

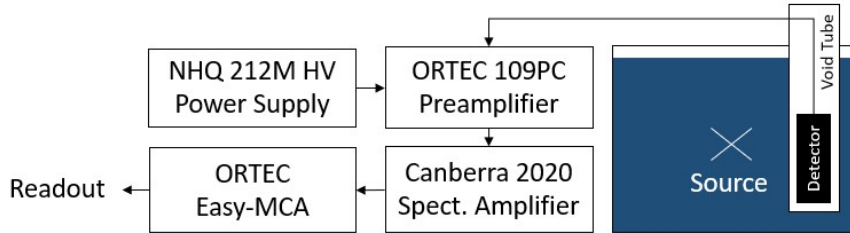


**Figure 7:** Experiment Block Diagram

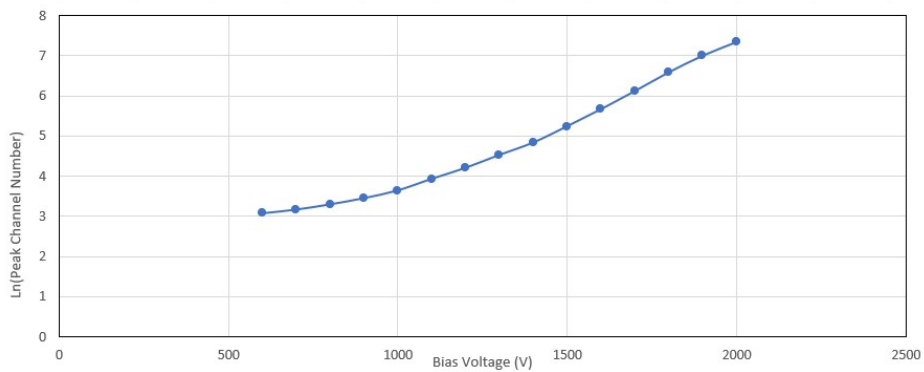


**Figure 8:** Voltage Investigation

## 4.2 Extrapolation Distance

As stated in section 2.2.2, a suitable extrapolation distance away from the boundaries should be decided upon (using Equation 10) in order bound the measurement and fitting cases. Using the thermal-group constant  $D$  of 0.16 provided by Lamarch & Baratta [13], Equation 16 calculates the appropriate extrapolation distance for this experiment. Clearly an extrapolation distance of 0.34cm is much smaller than the expected values of  $L$  and this region is not in danger of being measured given the slider mechanism and detector geometries, further comment shall be made in the results and analysis section.

$$d = 2.14 \times 0.16 = 0.34\text{cm} = 3.4\text{mm} \quad (16)$$

## 4.3 Radial $\text{BF}_3$ Measurements

The detector was seated on the bottom of the void tube and measurements were taken from 100mm → to 480mm, every 20mm. A run-time of 100s was used, producing a dead-time of <5%. The initial distance of 100mm was chosen as it was one of the closest measurable points on the sliding scale attached to the top of the tank. These measurements were then repeated with the Cadmium sheath fitted. Taking measurements every 20mm produced a total of 21 measurements, a small number of these (without cadmium sheath) are plotted below on Figure 9 in order to illustrate the reduction in counts as the detector is moved away from the source.

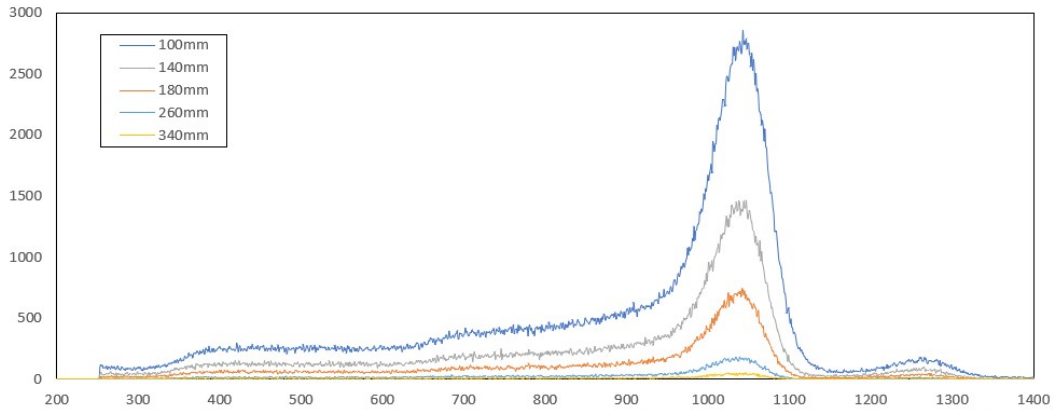


**Figure 9:** Sample of the spectra recorded for radial displacement of the detector

#### 4.4 Axial $\text{BF}_3$ Measurements

A total of 25 axial measurements were taken at a fixed radial position of 240mm, from -60mm → to 420mm, every 20mm. A run-time of 100s was again used. These measurements were repeated with the Cadmium sheath fitted. Again, a small number of the measurements taken are plotted on Figure 10. It was noted that counts dropped severely with increasing distance from the source, but less severely with increasing void. This small change in counts due to increasing void at the bottom of the detector is likely due to the small area presented for detection by the bottom of the detector tube, especially when this area is compared to the circumference of the cylindrical geometry.

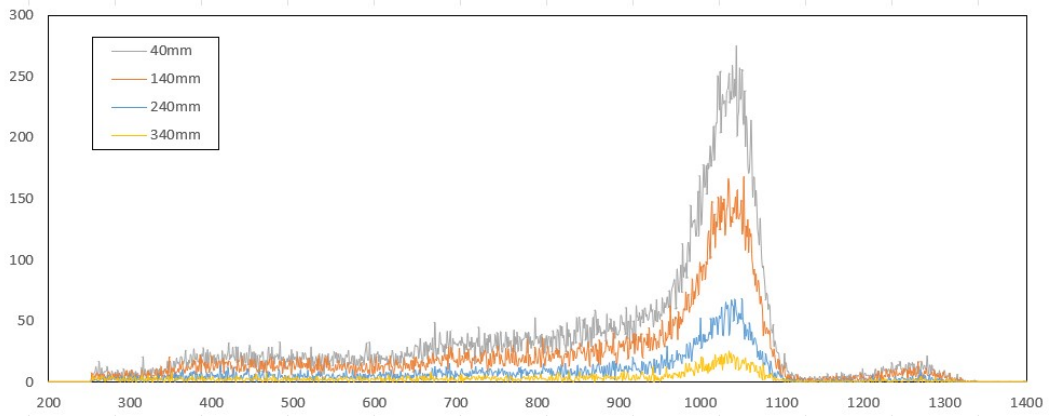


**Figure 10:** Sample of the spectra recorded for axial displacement of the detector

#### 4.5 ${}^3\text{He}$ Measurements

The equipment was powered down,  $\text{BF}_3$  detector was disconnected, and the  ${}^3\text{He}$  detector was connected. The voltage increased to 1400V in order to bring the detector into the proportional operating region. A total of 19 measurements were taken, these were a mixture of measurements taken as both axial and radial distances were varied. A small number of measurements were taken with the detector at the bottom of the void tube, every 50mm from 100mm → 200mm. The latter of the measurements were for verification of the diffusion length ( $L$ ). There measurements were repeated with the Cadmium sheath fitted around the detector.

## 4.6 Energy Calibration

To select a suitable region of interest (ROI) for the collection of counts given neutrons incident on the detector, an energy calibration (Figure 11) was conducted by measuring the centroid position of the 2.31 MeV and 2.79 MeV peaks. The Gaussian fitting software used in order to attain the centroid positions is detailed fully in the author's previous laboratory report [4]. The lower bound of the maestro ROI may then be calculated using the equation produced by the linear least-squares fit. The lowest energy of interest is the energy deposited in the detector due to the wall effect, i.e. 4/11ths of the full energy peak, which is 0.84 MeV [12] (as shown by Figure 4b). The lower error bounds were used on  $m$  and  $c$  to get the lowest possible centroid position of 358. Visibly, this was reduced to 320 given the full-width half max of this peak on the spectrum. The upper bound of the ROI was set to encompass the highest energy peak (2.79 MeV) at 1400.

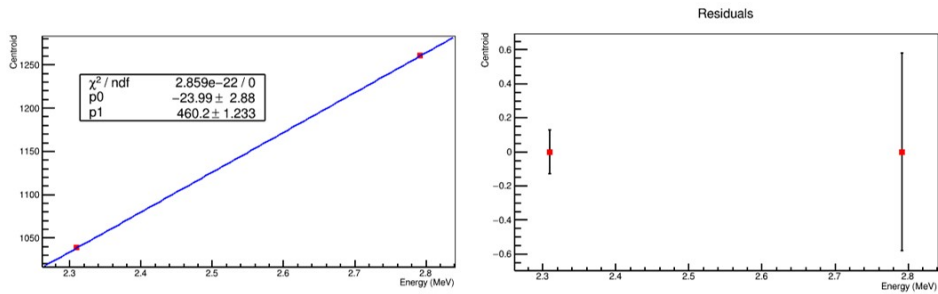


**Figure 11:** Sample of the spectra recorded for radial displacement of the detector

## 4.7 Least Squares Fitting

The counts encompassed by the Maestro ROI (as previously set) were put into Microsoft Excel for both Cadmium shielded measurements and non-shielded measurements. From thus, the errors on the counts were ascertained by taking the square root of the measurements (Poisson statistics). The flux (counts per second) was then calculated by dividing the counts by the live time (100s, from section 4.3). The thermal and fast fluxes were then split according to the Cadmium cut-off energy, where the fast flux is simply the counts recorded with the Cadmium sheath fitted, the thermal flux is the measured count rate without the sheath minus the flux with the sheath fitted. Once the thermal and fast fluxes had been split atten-

tion turned to the distance from the source to the detector. When the detector is at the bottom of the void tube the neutron count rate was not at maximum, only when the detector was drawn out by 60mm (axially) was the center of the detector roughly in line with maximum point of flux. To correct for this the straight line distance was used, i.e.  $\sqrt{radial^2 + axial^2}$ .

An Excel fit between the total (one group), thermal and fast (two group) flux and distance from the detector was conducted using the solver add-in. This gave a quick estimate of the one and two group fit constants of  $L$ ,  $\tau$ ,  $C$ , and  $A$  from Equations 4 and 6. Least squares fitting was conducted on the resultant single and two (fast and thermal) fluxes plotted as a function of distance from detector using the ROOT analysis software on the university Linux server. In order to achieve this the supplied LSF.C [2] code was altered (replacing "pow", previously a power fit) to fit for neutron flux, Appendix B shows the applicable changes in code. Initial guesses generated by the Excel solver fits were used as the initial parameters.

#### 4.8 MCBEND Comparison

A simplified model (shown by Figure 12) was constructed using measurements of the water tank and detector used. A point source was located at a location of Xmm within the tank, at a source intensity of  $2.59 \times 10^6$  neutrons per second (Equation 15). The tank was taken as a cylinder and does not reflect the shape of the water tank exactly, but is deemed as a reasonably good approximation. Polypropylene was used as the tank material. The neutron flux was scored at the same source to distance measurements as the experimentally measured fluxes with the  $\text{BF}_3$  detector. The dose rate at the tank boundary was also simulated (out of interest) and was found to be  $0.6136 \mu\text{Sv}/\text{hr}$  at a 2.2% certainty.

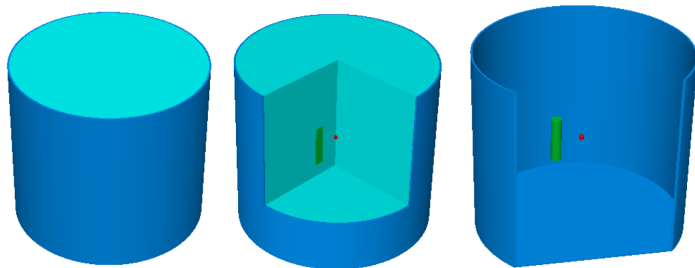


**Figure 12:** MCBEND Geometry

## 5 Results and Analysis

The fitted (Figure 15 fit) thermal neutron flux was taken and fed into a python heat map code, producing Figure 13. This heat map confirms that the point of maximum flux is at approx. 60mm from the bottom of the detector tube. It also evident that neutrons are diffused very readily in the medium (water), thermal flux is reduced to a figure of tens of counts per second incident on the detector at the extremities of the tank.

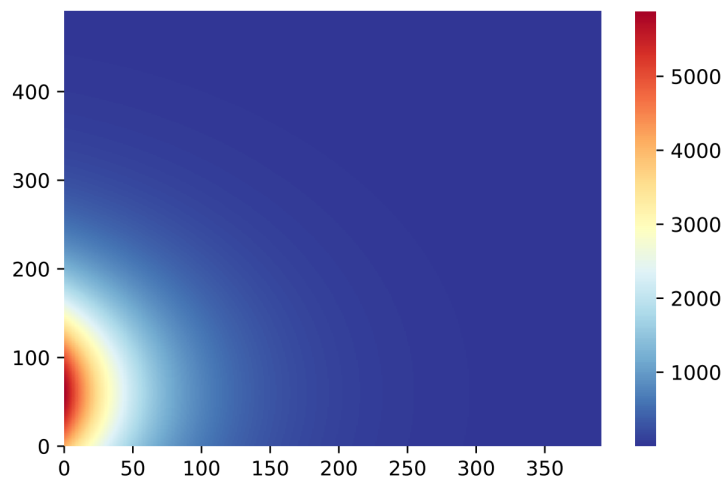


**Figure 13:** Fitted thermal neutron heat map

The fast neutron (Equation 4) flux against distance fit is shown on the left of Figure 14. A  $\chi^2/\text{ndf}$  value of  $94.68/18$  rejects the null hypothesis for a 5% significance level, which is no surprise given the apparent accuracy of this two-group model. Using the  $\chi^2$  test for a goodness of fit on a non-linear model is not necessarily appropriate. On the residuals plot (Figure 14) there is no apparent under-laying pattern, but the flux measured close to the source does not fit the expected model when compared to the other data points. This still holds true as those closest measurements are removed, therefore the model is less accurate at high fluxes and smaller distances. The fast neutron age ( $\tau$ ) was found to be  $4616 +/- 102.4\text{mm}^2$ , this is a large discrepancy when compared to the predicted result of  $5871 +/- 260\text{mm}^2$  of Iqbal and Mirza et al [10]. The main influencing factor in this result may be the lack of counts associated with neutrons above the cadmium cut-off energy (fast), a more accurate result may be achieved by increasing the measurement time and water volume.

For the two group thermal fit the flux-distance fitted plot is shown by Figure 15. The residuals plot shows large errors with the first three high flux points on the fitted plot. The constant (C) is a negative value for (Equation 6) as predicted in Section 2.2. The thermal neutron diffusion length ( $L$ ) was shown to be a value of  $26.16 \pm 0.46$  mm. This is not within the error bounds of the predicted value supplied by Iqbal and Mirza el al [10] of  $29.49 \pm 1.3$ mm, nor within the bounds of the figure retrieved from Holmes and Zerkle et al [9] ( $27.61 \pm 0.09$ mm). The use of reactor grade pure water in the Iqbal and Mirza el al [10] may affect the diffusion of neutrons, and even small sources of voidage can affect the diffusion of neutrons in a detrimental way [10]. Alternative measurement spacing and differences in experiment geometry may also play a part in experimental differences. The evaluated study results within the Holmes and Zerkle et al [9] paper show large discrepancies between experimental results for diffusion length ( $L$ ) in the  $20^{\circ}\text{C}$  range.

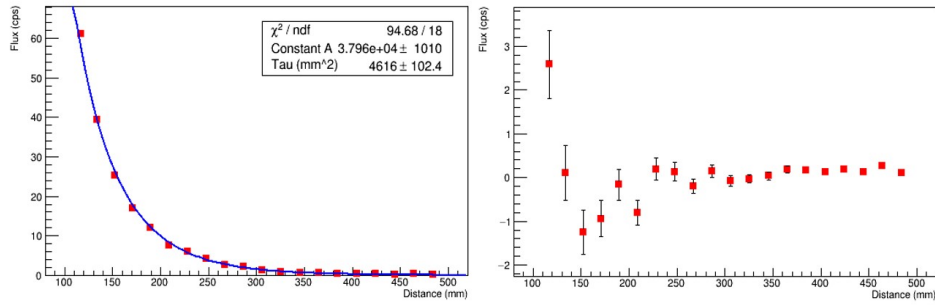


**Figure 14:**  $\text{BF}_3$  Two group fast neutron fit using Code Listing 3

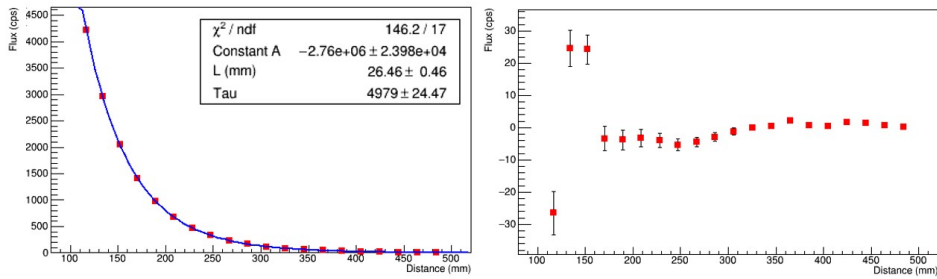


**Figure 15:**  $\text{BF}_3$  Two group thermal neutron fit using Code Listing 4

Only four measurements could be fitted to a reasonable degree of accuracy with the results of the  ${}^3\text{He}$  detector investigations. The flux-distance plot for a two group thermal fit is shown by Figure 16. The fitted thermal diffusion length ( $L$ ) was found to be  $26.16 \pm 0.73$ mm, this is comparable to the result attained in the  $\text{BF}_3$

experiment (Figure 15) with both lower and upper error bounds crossing.

The results of the MCBEND simulation were plotted against the fitted neutron flux and measured neutron flux (Figure 17). The thermal flux ( $<0.5\text{eV}$ ) of the MCBEND follows the same trend as the both the fit and measured fluxes, but with the fluxes slightly lower on the MCBEND results at  $>100\text{mm}$ , possibly due to the lack of background neutrons in the MCBEND model and other physical errors present. The plot of residuals show a large error between the fitted data and MCBEND results at the high flux/close distance region, this suggests poor cohesion of the two group neutron diffusion model at distances close to the source.

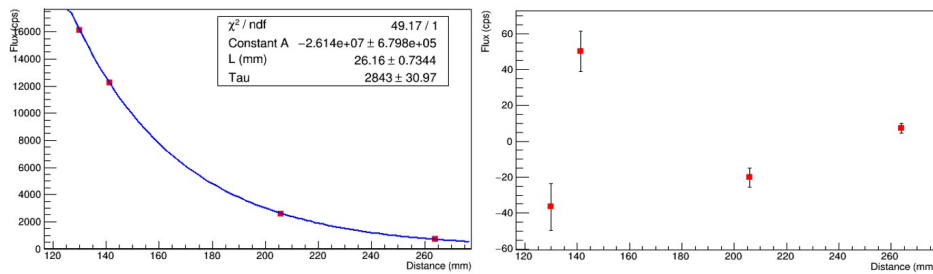


**Figure 16:**  ${}^3\text{He}$  Two group thermal neutron fit using Code Listing 4

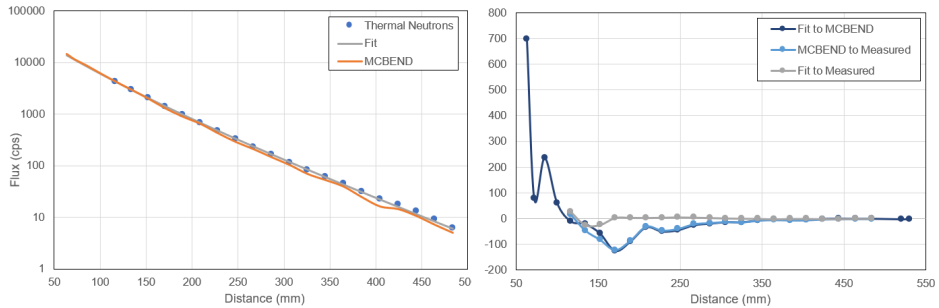


**Figure 17:** MCBEND Results plotted against measured and fit results.

The region close to the tank boundary is illustrated by Figure 18. From this plot it can be seen that the MCBEND flux drops severely as it approaches the surface of the tank, analogous to the exact flux in Figure 2. The fitted flux remains unaffected by the presence of the container wall, as anticipated given the assumption of an infinite medium by the diffusion theory applied. It can also be seen that measurements were not taken near to the boundary, therefore the fit remains unaffected by this behaviour at the container wall.

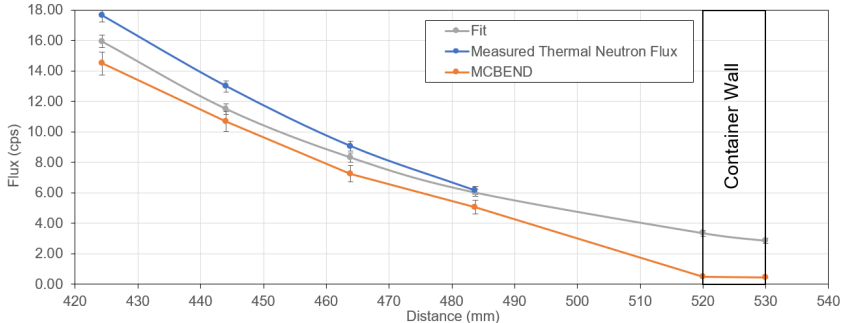


**Figure 18:** MCBEND thermal flux comparison

## 6 Conclusion

Both values of fast neutron age ( $\tau$ ) ( $4616 +/- 102.4\text{mm}^2$ ) and diffusion length ( $L$ ) ( $26.16 +/- 0.46 \text{ mm}$ ) do not meet or lie within the error bounds of the values ascertained from literature [10] [9]. This result meets the expectation of Lamarsh & Baratta [13]; the two group approximation used herein is not a particularly accurate model to use. Further complications arise from the secondary use of the tank as an neutron activation bath, unknown samples could potentially be the source of additional  $\gamma$ 's which may affect the measurements adversely. Activation products within the moderator may also be a source of unwanted noise. Geometry and measurement spacing will also impact the fitted results. It is encouraging however that the results were of a similar magnitude of the literature values. There were a low number counts attained for the fast neutrons, to improve this the measurements from the  $\text{He}^3$  detector should have been improved upon, along with the measurement time. Corrections due to detector efficiencies may have also been applied to improve upon the result and converge on the literature values. Investigating the behaviour of the two group fit using a comparison against MCBEND illustrates the assumptions made by diffusion theory and how might they be mitigated in order to achieve a representative result.

## Acknowledgements

Much of the trouble-shooting and technical guidance came from Prof. Peter Jones, Dr. Dave Forest, Dr. Paul Norman, and Pedro Santa Rita Alcibia during this experiment. This experiment was conducted jointly with my lab partner for this semester, Georgij Liasenko. I'd like to thank those involved for the support throughout.

## References

- [1] R. Bedogni et al. “Investigation of the neutron spectrum of americium–beryllium sources by Bonner sphere spectrometry”. In: *Nuclear Instruments and Methods in Physics Research Section A: Accelerators, Spectrometers, Detectors and Associated Equipment* 763 (2014), pp. 547–552. ISSN: 0168-9002. DOI: <https://doi.org/10.1016/j.nima.2014.06.040>. URL: <https://www.sciencedirect.com/science/article/pii/S0168900214007633>.
- [2] University of Birmingham Dept. of Physics and Astronomy. *ROOT Analysis Framework*. URL: <https://canvas.bham.ac.uk/courses/60469/pages/root-analysis-framework>. Date Accessed: 01 May 2022.
- [3] Brookhaven National Nuclear Data Center. *NuDat 3.0*. URL: <https://www.nndc.bnl.gov/nudat3/>. Date Accessed: 08 March 2022.
- [4] Benjamin Crump. *Experimental Analysis of X-Ray Fluorescence: A University of Birmingham Lab Report*. Tech. rep. 2022. URL: <https://github.com/you-shall-not-parse/uob-nuclear-msc>.
- [5] Benjamin Crump. *github repository*. URL: <https://github.com/you-shall-not-parse/uob-nuclear-msc>. Date Accessed: 15 April 2022.
- [6] James J. Duderstadt and Louis J. Hamilton. *Nuclear Reactor Analysis*. 1977. DOI: 10.1109/TNS.1977.4329141.
- [7] GRAF. *Rainwater Tanks*. URL: <https://www.graf-water.co.uk/rainwaterharvesting/rainwater-tanks/top-tank.html>. Date Accessed: 12 April 2022.
- [8] HyperPhysics.phy GSU. *Particles: Protons and Neutrons*. URL: <http://hyperphysics.phy-astr.gsu.edu/hbase/Particles/proton.html>. Date Accessed: 08 March 2022.
- [9] Jesse C. Holmes, Michael L. Zerkle, and Ayman I. Hawari. “Validation of Thermal Scattering Laws for Light Water at Elevated Temperatures with Diffusion Experiments”. In: *European Physical Journal Web of Conferences*. Vol. 247. European Physical Journal Web of Conferences. Apr. 2021, 09016, p. 09016. DOI: 10.1051/epjconf/202124709016.
- [10] Masood Iqbal, Nasir M Mirza, and Sikander M Mirza. “Experimental study of effect of void volume fraction on neutron diffusion parameters in water”. In: *Radiation Physics and Chemistry* 64.5 (2002), pp. 349–357. ISSN: 0969-806X.

- DOI: [https://doi.org/10.1016/S0969-806X\(01\)00613-2](https://doi.org/10.1016/S0969-806X(01)00613-2). URL: <https://www.sciencedirect.com/science/article/pii/S0969806X01006132>.
- [11] ISO 8529-1. Reference neutron radiations, Part 1: Characteristics and methods of production. International Organization for Standardization.
  - [12] Glenn F. Knoll. *Radiation Detection and Measurement*. 3rd. New York, NY: Wiley, 2000. URL: <https://cds.cern.ch/record/441925>.
  - [13] John R. Lamarsh and Anthony John Baratta. *Introduction to nuclear engineering*. 3rd ed. Upper Saddle River, N.J. : Prentice Hall, 2014.
  - [15] IAEA Nuclear Data Services. *Evaluated Nuclear Data File (ENDF) Database Version of 2022-03-30*. URL: <https://www-nds.iaea.org/exfor/endf.htm>. Date Accessed: 09 April 2022.

## Bibliography

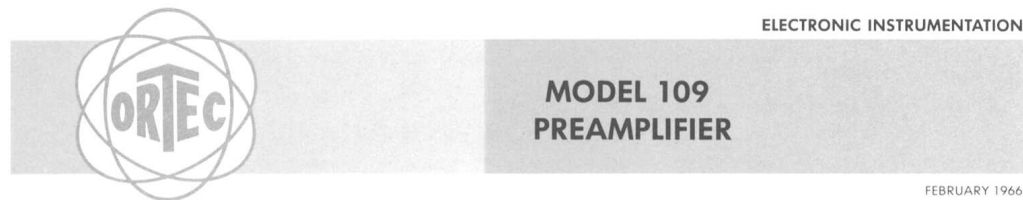
James J. Duderstadt and Louis J. Hamilton. *Nuclear Reactor Analysis*. 1977. DOI: 10.1109/TNS.1977.4329141.

Glenn F. Knoll. *Radiation Detection and Measurement*. 3rd. New York, NY: Wiley, 2000. URL: <https://cds.cern.ch/record/441925>.

John R. Lamarsh and Anthony John Baratta. *Introduction to nuclear engineering*. 3rd ed. Upper Saddle River, N.J. : Prentice Hall, 2014.

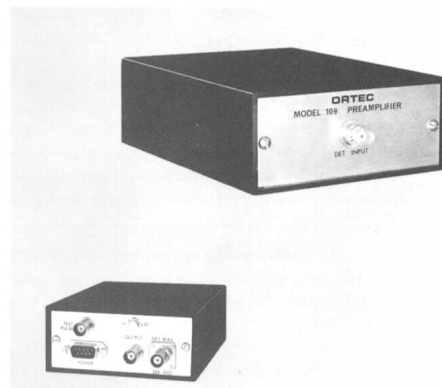
Louis Lyons. *A Practical Guide to Data Analysis for Physical Science Students*. Cambridge University Press, 1991. DOI: 10.1017/CBO9781139170321.

# Appendix A



## Features

- Field-effect transistor input stage
- Suitable for semiconductor and gas ionization counters
- All silicon transistors
- Output compatible with all shaping type main amplifiers
- Nonmicrophonic
- Charge-sensitive input circuit
- 10:1 gain change, switch selectable
- May be powered from ORTEC transistor main amplifiers or remote supplies



## Description

The ORTEC Model 109 Preamplifier is an all silicon transistor instrument which has been designed for semiconductor and gas ionization detectors. The unit is compatible with ORTEC transistor main amplifiers or other main amplifiers which provide signal pulse shaping. The printed circuit assembly is housed in an anodized extruded aluminum case.

## Specifications

Noise level, relative amplitude, and output pulse rise time are functions of the input capacitance due to the detector, cables, and connectors. Typical performance is tabulated below.

TYPICAL PERFORMANCE

Input cap. (pF)	Noise, with 1 $\mu$ sec RC Main Amp			Preamp output pulse	
	keV (fwhm,Si)	keV (fwhm,Ge)	rms electrons	Relative amplitude	Rise time (nsec) 10-90%
0	2.6	2.0	307	1.000	39
20	4.4	3.4	520	1.000	68
50	7.5	5.8	885	1.000	125
100	13.3	10.4	1570	.990	230
200	22.2	17.3	2620	.960	395

Warranty basis:  $\leq 2.9$  keV Si at 0 pF external capacitance

Output pulse shape: Rise time as in table above; exponential fall with 50  $\mu$ sec time constant

Integral nonlinearity:  $\leq 0.1\%$  for 0-1.5V output span

Temperature coefficient:  $\pm 0.01\%$  per  $^{\circ}$ C

Detector bias isolation: 1000V dc

Input open loop gain: >5000

Power required: +24 dc at 15 mA, -24V dc at 15 mA; supplied from ORTEC main amplifier or remote supply

Cable required: 10-foot compatible cable supplied with preamplifier

Power connector: Amphenol 17-20090

Saturated output amplitude: 7V at end of several hundred feet of unterminated 93-ohm cable

Output source impedance: Adjustable from 50 to 150 ohms

Charge sensitivity: 150 mV/MeV in  $\times 10$  gain position  
15 mV/MeV in  $\times 1$  gain position

Detector, output, and test pulse connectors: BNC

Detector bias connector: MHV

Size: 1.75  $\times$  4  $\times$  6 inches (4.45  $\times$  10.2  $\times$  15.3 cm)

Weight: Net, 1.5 pounds (0.68 kg); gross, 2.3 pounds (1.05 kg)

OAK RIDGE TECHNICAL ENTERPRISES CORPORATION, PO. BOX C, OAK RIDGE, TENNESSEE • PHONE (615) 483-8451



## MODEL 109PC PREAMPLIFIER MODIFIED FOR PROPORTIONAL COUNTERS

FEBRUARY 1966

### Specifications

The ORTEC Model 109PC Preamplifier is a special version of the standard Model 109, containing circuit revisions that make it suitable for use with proportional counters used in low energy x-ray or gamma-ray spectrometry. The modifications consist of changes in the input circuit connector and capacitors so as to accommodate up to 3000 volts bias on the counter, a longer clipping time, and a reduction in the value of the detector load resistor so as to minimize counter voltage variations with signal current. These modifications result in poorer noise performance of the preamplifier compared to the standard version; however, the resultant performance with the proportional counter is superior (~355 rms electrons at 0 pF; slope, 9.4 electrons per pF).

This modified preamplifier is intended for application with proportional counters such as the Reuter-Stokes RSG-30A for such purposes as low energy x-ray or gamma-ray spectrometry or counting where the theoretical limit of energy resolution is desired. It has been found in some proportional counter tubes that at high gas amplification factors there may be a significant shift in peak position with simultaneous peak broadening due to space charge effects. For example,\* with the Reuter-Stokes RSG-30A proportional counter tube with 90% xenon, 10% methane gas operating at applied voltage of 2400 volts and a source of AgK $\alpha$  (22.16 keV) x-rays, as the count rate is changed from a few counts per second to about 5000 counts per second, the peak position shifts approximately the full width at half maximum (fwhm) of the peak. A satisfactory method for reducing this effect to within acceptable limits is to reduce the gas amplification factor considerably. This, in turn, reduces the output signal from the proportional counter tube so drastically that a low noise preamplifier such as the Model 109PC is necessary to amplify the signal. Gratifying improvement is achieved over cathode followers or white follower circuits which are usually quite noisy when compared with a low noise preamp such as the Model 109PC.

Note that the Model 109PC provides pulse shaping consisting only of a 200-microsecond time constant single clip, for pileup prevention in the preamplifier. It must be followed by a suitable shaping type main amplifier such as the ORTEC Model 410.

Charge gain of the 109PC is  $3.36 \times 10^{12}$  volts/coulomb ( $0.540 \times 10^{-6}$  volts/electron or 150 mV/MeV with silicon solid state detectors), reducible one-tenth by the gain switch. The detector load resistor is 22 megohms.

\*Reference: R. W. Hendricks, to be published.



22266R/P

ORTEC's products include SEMICONDUCTOR CHARGED PARTICLE DETECTORS, NEUTRON SPECTROMETERS and DETECTORS, dE/dx COUNTERS, LOW NOISE BIASED AMPLIFIER SYSTEMS, LABORATORY STANDARD PULSE GENERATORS, SUM-COINCIDENCE UNITS, ION SOURCES, ION and PLASMA PHYSICS PRODUCTS, and RADIOACTIVE SOURCES.

## Appendix B

```
...case 4:  
    func = new TF1("pow", "[0]*x**[1]");  
    func->SetParameter(0,1.);  
    func->SetParameter(1,1.);  
    func->SetParName(0,"Constant");  
    func->SetParName(1,"Exponent");  
    g->Fit("pow");  
    func = g->GetFunction("pow");  
    break; ...
```

**Code Listing 1:** Regular power fit of the un-edited LSF.C file.

```
...case 4:  
    func = new TF1("pow", "[0]/x*exp(-x/[1])");  
    func->SetParameter(0,25000);  
    func->SetParameter(1,70);  
    func->SetParName(0,"Constant A");  
    func->SetParName(1,"L (mm)");  
    g->Fit("pow");  
    func = g->GetFunction("pow");  
    break; ...
```

**Code Listing 2:** For completeness, LSF.C edited (LSFSG.C) for a single neutron group solution for flux, i.e. Equation 4 but with  $\sqrt{\tau}$  replaced by  $L$  to solve for total flux ( $\phi$ ).

```
...case 4:  
    func = new TF1("pow", "([0]/x)*(exp(-x/sqrt([1])))");  
    func->SetParameter(0,35415);  
    func->SetParameter(1,4791);  
    func->SetParName(0,"Constant A");  
    func->SetParName(1,"Tau (mm^2)");  
    g->Fit("pow");  
    func = g->GetFunction("pow");  
    break; ...
```

**Code Listing 3:** LSF.C edited (LSFSGF.C) for a two neutron group solution for fast neutron flux i.e. Equation 4.

```

... case 4:
    func = new TF1("pow", "([0]/x)*(exp(-x/[1])-exp(-x/sqrt([2])))");
    func->SetParameter(0,-2752989);
    func->SetParameter(1,29.49);
    func->SetParameter(2,5871);
    func->SetParName(0,"Constant A");
    func->SetParName(1,"L (mm)");
    func->SetParName(2,"Tau");
    g->Fit("pow");
    func = g->GetFunction("pow");
    break; ...

```

**Code Listing 4:** LSF.C edited (LSFTG.C) for a two neutron group solution for thermal neutron flux i.e. Equation 6.